Numerical Models of Shear-Induced Melt Band Formation with Anisotropic Matrix Viscosity

S.L. Butler[a,*]

[a]*Department of Geological Sciences, University of Saskatchewan, 114 Science Place, Saskatoon, SK, S7N 5E2, Canada*

Abstract

When a system of partial melt is subjected to an externally driven strain-rate, an instability can occur whereby bands of low and high porosity form. Theory and numerical simulations have shown that if the matrix viscosity is isotropic and strain-rate independent, the bands grow fastest when parallel to the direction of maximum compression of the externally imposed flow. However, experiments indicate that bands form at angles that differ by roughly 25° from the direction of maximum compression even when the matrix viscosity is strain-rate independent. Recently, *Takei and Holtzman* (2009c) have argued that the matrix viscosity is likely to be anisotropic when partial melt is present because of the anisotropic arrangement of melt at the grain scale. These authors also presented a theoretical expression for the stress tensor in the presence of this anisotropy and a linear theory of band formation that indicated that bands would form at angles that are in accord with the results of experiments. In this contribution, I present the results of linear theory and full nonlinear simulations of band formation under simple shear with anisotropic viscosity. I show that, even when the viscosity is strain-rate independent, the resulting bands form at low angles in accord with experiments if the anisotropy reflects a distribution of melt in pockets aligned parallel to the direction of maximum compression. If instead the anisotropy represents melt that is aligned at low angles to the shear plane, as seen in highly deformed experiments, the melt bands rapidly rotate to high angles. In that case, another mechanism is required to maintain the bands at low angles. The effects of buoyant melt are also investigated and bands are shown

*Corresponding author. Fax:+1-306-966-8593

Email address: sam.butler@usask.ca (S.L. Butler)

to grow at the same rate as when buoyancy is absent, but with an additional secondary preferred orientation.

Keywords: viscous anisotropy, compaction, melt band

1. Introduction

A porosity-localizing instability will occur in a partially molten system that is subjected to an externally imposed strain rate if the solid matrix is modeled as a very viscous fluid whose viscosity decreases with porosity and if the system size is greater than the compaction length of the material. This instability was first predicted theoretically by *Stevenson* (1989) and was demonstrated numerically for a system undergoing pure shear by *Richardson* (1998). Laboratory experiments in which partially molten samples undergo simple shear have demonstrated that porosity bands form at an angle of roughly 20° to the shear plane (*Holtzman et al.*, 2003; *Holtzman and Kohlstedt*, 2007; *Kohlstedt et al.*, 2009; *King et al.*, 2010) regardless of the strain-rate dependence of viscosity (*Kohlstedt and Holtzman*, 2009). This is in contrast to the predictions of linear theory (*Spiegelman*, 2003; *Rabinowicz and Vigneress*, 2004; *Katz et al.*, 2006) and numerical simulations (*Katz et al*, 2006; *Butler*, 2009) that indicate that when viscosity is strain-rate independent, bands grow fastest at 45° to the shear plane (parallel to the direction of maximum compression) and occur at lower angles when viscosity is strongly strain-rate dependent.

When partially molten samples are sheared, melt at the grain scale becomes aligned in large aspect ratio pockets in orientations that are controlled by the stress field (*Daines and Kohlstedt*, 1997; *Zimmerman et al.*, 1999; *Kohlstedt and Holtzman*, 2009). In experiments approximating pure shear, the melt pockets become aligned parallel to the direction of maximum compression (*Takei*, 2005, 2010). As a result, there will be less contact and hence less resistance to grain-boundary diffusion between grains in the direction perpendicular to the direction of maximum compression leading to viscosity that depends on the orientation of the stress field. However, at larger strains in simple shear experiments, the melt pockets become aligned at roughly 20° to the shear plane leading to a different orientation of viscosity anisotropy (*Zimmerman et al.*, 1999).

The melt extracted at mid-ocean ridges emerges within roughly 1 km of the ridge axis (*Vera et al.*, 1990) while seismic evidence indicates that there

is melt over a lateral distance of roughly 100 km at 60 km depth (*Forsyth et al.*, 1998). Also, the melt extracted at mid-ocean ridges is not in equilibrium with the rock through which it has passed (*Kelemen et al.*, 1997). These observations require a mechanism to both focus the melt towards the ridge axis and carry it rapidly. *Katz et al.* (2006) showed that if melt bands are rotated relative to the orientation for maximum compression, as they are in laboratory experiments, then they are in a good orientation to act as high permeability conduits to carry melt towards the ridge axis. As a result, it is potentially very important to our understanding of Earth's interior that we understand why bands in experiments are found at low angles to the shear plane.

When the melt is buoyant compared with the matrix, the fluid can rise, leading to oscillations and waves (*Spiegelman*, 1993). *Butler* (2009) simulated the formation of melt bands in the presence of buoyancy-induced oscillations and found that bands continued to form and grew at essentially the same rate as in the absence of buoyancy. When the matrix viscosity used was strain-rate dependent, a second set of higher angle bands also became apparent. However, *Katz* (2010) modeled melt extraction at a mid-ocean ridge and melt bands were not observed despite the fact that porosity weakening viscosity was used in his model.

In what follows, I first describe the matrix viscosity model used here which employs the formulation of *Takei and Holtzman* (2009c). Subsequently, I describe the numerical model and outline the linear theory that predicts the growth rate and oscillation frequency as a function of melt band orientation. In section 5, I present the results of the numerical modeling and the predictions of linear theory first for static anisotropy and then for anisotropy that changes with time. I then investigate the effects of buoyancy with viscous anisotropy. I end with a discussion of the significance of these results.

2. Viscosity Model

Takei and Holtzman (2009c) derived the following expression relating the components of the deviatoric stress tensor, $\boldsymbol{\sigma}$, to the components of the strain-rate tensor, $\dot{\epsilon}$,

$$\begin{pmatrix} \sigma_{xx} \\ \sigma_{yy} \\ \sigma_{xy} \end{pmatrix} = \begin{pmatrix} \xi+\eta+\zeta_1+2\zeta_2 & \xi-(\eta+\zeta_1) & 2\zeta_3 \\ \xi-(\eta+\zeta_1) & \xi+\eta+\zeta_1-2\zeta_2 & 2\zeta_3 \\ \zeta_3 & \zeta_3 & 2(\eta-\zeta_1) \end{pmatrix} \begin{pmatrix} \dot{\epsilon}_{xx} \\ \dot{\epsilon}_{yy} \\ \dot{\epsilon}_{xy} \end{pmatrix} \tag{1}$$

Here, $\epsilon_{xx} = \frac{\partial U}{\partial x}$, $\epsilon_{yy} = \frac{\partial V}{\partial y}$ and $\epsilon_{xy} = \frac{1}{2}(\frac{\partial U}{\partial y} + \frac{\partial V}{\partial x} + 1)$ where U and V are the velocities of the solid matrix in the x and y directions. In what follows, gravitational acceleration is assumed to act in the direction of increasing $-y$. The bulk and shear viscosities are represented by ξ and η while the anisotropy components are represented by ζ_1, ζ_2 and ζ_3.

A 2D circular grain model was developed by *Takei and Holtzman* (2009c), and parameters Θ_k characterized the angular extent of eight regions around the grain as to whether they were in contact with the neighboring grain. The total angular extent of the outer boundary of the grain that is in contact with its neighbours is referred to as the total contiguity. This model is shown conceptually in figures 1a and b for type A and B anisotropy which will be defined shortly. Full contact implies $\Theta_k = \pi/8$ while the mean contact angle for an isotropic case as given by these authors is $\Theta_1^0 = \pi/8(1 - 2\phi_0^{0.5})^{0.5}$. When the initial porosity, $\phi_0 = 0.01$, as is assumed here, $\Theta_1^0 = 0.3512$. The Θ_k are then used to derive expressions η, ξ, ζ_1, ζ_2 and ζ_3. The symmetry $\Theta_k = \Theta_{k+4}$ for $k = 1$ to 4, is also assumed.

In the following analysis, the porosity dependence of all of the viscosity components will be assumed to be the same. The shear viscosity takes the form $\eta = \eta^0 \exp[\alpha(\phi - \phi_0)]$, where $\alpha = -25$ (*Mei et al.*, 2002) and ϕ is the porosity. All of the other viscosity components are assumed to be proportional to η, i.e., $\xi = \xi^0\eta$ and $\zeta_i = \zeta_i^0\eta$ for $i = 1 - 3$. All of the viscosity components are nondimensionalized by the initial shear viscosity, η^0. The dimensionless bulk and anisotropic viscosity coefficients then become (*Takei and Holtzman*, 2009c)

$$\xi^0 = \frac{\frac{2}{3}\sum_{k=1}^{4}(2\Theta_k)^3}{\sum_{k=1}^{4}(2\Theta_k - \frac{1}{2\Theta_k}\sin^2(2\Theta_k))}, \tag{2}$$

$$\zeta_1^0 = \frac{\sum_{k=1}^{4}(-1)^{k+1}(\sin(4\Theta_k) - \frac{1}{\Theta_k}\sin^2(2\Theta_k))}{\sum_{k=1}^{4}(2\Theta_k - \frac{1}{2\Theta_k}\sin^2(2\Theta_k))}, \tag{3}$$

$$\zeta_2^0 = \frac{4\Theta_2\cos(2\Theta_2) - 2\sin(2\Theta_2) - 4\Theta_4\cos(2\Theta_4) + 2\sin(2\Theta_4)}{\sum_{k=1}^{4}(2\Theta_k - \frac{1}{2\Theta_k}\sin^2(2\Theta_k))}, \tag{4}$$

$$\zeta_3^0 = \frac{-4\Theta_1\cos(2\Theta_1) + 2\sin(2\Theta_1) + 4\Theta_3\cos(2\Theta_3) - 2\sin(2\Theta_3)}{\sum_{k=1}^{4}(2\Theta_k - \frac{1}{2\Theta_k}\sin^2(2\Theta_k))}. \quad (5)$$

The superscript 0 indicates a quantity evaluated at the initial porosity, ϕ_0.

When an external stress is imposed, melt around grains becomes distributed preferentially in large aspect ratio pockets with long axes parallel to the direction of maximum compression (*Takei*, 2005, 2010). In all of the numerical simulations presented here, a background velocity of the form $\mathbf{U_0} = \dot{\gamma} y \hat{i}$ is imposed, where $\dot{\gamma}$ is the strain rate and $\hat{i}$ is a unit vector in the horizontal direction. The equation above describes a simple shear flow for which the direction of maximum compression, σ_1, is in the $(1/\sqrt{2}, -1/\sqrt{2})$ direction if the viscosity is constant. When this happens, contact is reduced between grains with tangent in the direction of maximum extension, σ_3, so $\Theta_1 = \Theta_5$ become less than Θ_1^0 while all other contacts are unchanged for the imposed flow geometry. This situation is represented graphically in figure 1a for the case of $\Theta_1 = \Theta_5 = 0$. *Takei and Holtzman* (2009c) referred to this as type A anisotropy and this term will be maintained here. Using the formulas above and taking the extreme case that $\Theta_1 = \Theta_5 \ll \Theta_1^0$, I get values for the bulk viscosity at the initial porosity, $\xi^0 = 2.1357$, and for the anisotropy coefficients, $\zeta_1^0 = 0.3115$, $\zeta_2^0 = 0$ and $\zeta_3^0 = -0.6774$.

Zimmerman et al. (1999) found in their simple shear experiments that melt pockets had become aligned at roughly 20^0 to the shear plane. These experiments were sheared to 200% but it is likely that the change in melt alignment happened at a much smaller total shear. Again, I will follow *Takei and Holtzman* (2009c) and refer to this as type B anisotropy. This case is illustrated in figure 1b where contact is reduced for the grain boundaries with tangents dipping at shallow angles to the right. In the case shown, $\Theta_1 = \Theta_2 = \Theta_5 = \Theta_6 = 0.2$ while the other contact angles have value $\Theta_1^0 = 0.3512$. For these values, $\zeta_1^0 = 0$, $\zeta_2^0 = 0.6891$ and $\zeta_3^0 = -0.6891$.

In figure 2a, the viscosity coefficients are shown as a function of Θ_1/Θ_0^1. All other $\Theta_k = \Theta_0^1 = 0.3512$ and this represents the type A anisotropy case. The viscosity components have been normalized by the value of η^0 when Θ_1 approaches 0 and the values of the viscosity used in the simulations with type A anisotropy are taken from the $\Theta_1 = 0$ axis of this graph. As can be seen, the viscosity coefficients do not change significantly once $\Theta_1 < 0.3\Theta_0^1$.

Also, $\zeta_2^0 = 0$ for all type A anisotropy cases while ζ_1^0 is always positive and ζ_3^0 is always negative. The variation of the viscosity coefficients with $\Theta_1/\Theta_1^0 = \Theta_2/\Theta_1^0$ is shown in figure 2b. The thin vertical solid line indicates the value of $\Theta_1 = \Theta_2 = 0.2$ used in the type B simulations. The coefficients have been normalized by the value of η^0 at $\Theta_1 = \Theta_2 = 0.2$. As can be seen, ζ_1 is always 0 for type B anisotropy while ζ_2 and ζ_3 have equal magnitude but opposite sign.

In some simulations, the viscosity anisotropy was rotated continuously from type A to type B resulting in continuous changes in the viscosity coefficients. In all other simulations the viscosity coefficients were held constant throughout the simulation.

The axis of the imposed viscous anisotropy was fixed with respect to the simulation coordinates and did not rotate with a change in the stress orientation with viscous heterogeneity. As we will show, the orientations of the principle stress directions did not change very much over the course of a simulation from the orientations of principle strain-rate of the background simple shear flow indicating that this is a reasonable approximation for these calculations.

3. Governing Equations

Equations are scaled for length by the compaction length, $\delta_c = [k_0\eta^0(1+\xi^0)/\mu]^{0.5}$, for time by the inverse background strain-rate, $\dot{\gamma}^{-1}$, and for pressure by $p_0 = \eta^0(1+\xi^0)\dot{\gamma}$. Here, k_0 is the permeability at the initial porosity and μ is the liquid viscosity. Note that the porosity, ϕ, is not scaled. I employ the form of the equations of force balance and mass conservation for a compacting porous medium first derived by *McKenzie* (1984) which are similar to those of *Scott and Stevenson* (1984) and can be shown to be a special case of those given by *Ricard et al.* (2001).

$$\nabla \cdot \{\mathbf{U} - k_\phi[\nabla p - (1-\phi_0)B_u\hat{j}]\} = 0, \tag{6}$$

$$-\nabla p(1+\xi^0) + \nabla \cdot \boldsymbol{\sigma} = (\phi_0 - \phi)B_u(1+\xi^0)\hat{j}, \tag{7}$$

and

$$\frac{\partial \phi}{\partial t} = \nabla \cdot [(\mathbf{U} + y\hat{i})(1-\phi)]. \tag{8}$$

Here, $\mathbf{U}$ represents variations of the solid velocity from the background while p is the fluid pressure, $\hat{j}$ is a unit normal in the vertical direction

and t represents time. The permeability is taken to be isotropic with the form $k_\phi = (\phi/\phi_0)^3$ (*Wark and Watson*, 1998) . In the equations above, the transformed pressure, p, is related to the fluid pressure, p_{fluid}, by $p = p_{fluid} + B_u[(1-\phi_0)\rho_s + \phi_0\rho_l]y$ where ρ_s and ρ_l are the solid and liquid densities made dimensionless by dividing by the dimensional difference in density between the solid and liquid.

The buoyancy parameter, $B_u = (\Delta\rho g\delta_c)/(\dot{\gamma}\eta^0(\xi^0+1))$, characterizes the ratio of buoyancy to strain forces. Here $\Delta\rho$ is the density difference between the solid and fluid phases, and g is acceleration due to gravity.

Equations 7 with 1, as well as equations 6 and 8 were solved using the commercial finite element modeling package Comsol using the General PDE solver mode. For all calculations, a square domain with side lengths of 2 was used and 6282 triangular elements were used to mesh the box. The top and bottom boundaries were specified to be no-slip ($\mathbf{U} = 0$) and $p = 0$ while the side boundaries were periodic for the calculations with no buoyancy ($B_u = 0$). For the calculations with non-zero B_u, the top and bottom boundaries were specified to be periodic as well. Equation 8 can be expanded as

$$\frac{\partial\phi}{\partial t} + y\frac{\partial\phi}{\partial x} + \mathbf{U}\cdot\nabla\phi = (1-\phi)\nabla\cdot\mathbf{U}. \tag{9}$$

where the second term on the left-hand side represents the advection of the porosity field by the background velocity field and the term on the right-hand side represents compaction (*Spiegelman*, 2003) . The third term on the left represents the advection of the porosity field by the velocity variation from the background and it tends to be small. Because of the simple shear background flow, there is a discontinuity in the advection rate of the porosity field by the background flow going from the top boundary to the bottom one. For calculations with B_u of 1 or greater, the effects of compaction dominate those due to advection by the background flow and equation 8 remains satisfied on the boundary despite the discontinuity in the advection rate.

The initial porosity was of the form $\phi = \phi_0 + \Delta\phi f(x,y)$ where ϕ_0 and $\Delta\phi$ were 0.01 and 10^{-8} for all calculations. The perturbation function, $f(x,y)$, was calculated as the inverse fourier transform of a gaussian function with a standard deviation of $10\sqrt{2}$ and random phase. This created a random initial condition with wavelengths significantly greater than the grid spacing.

4. Linear Theory

Equations 6, 7 and 8 can be expanded keeping only terms of first order. Gravity is assumed to act in the $-\hat{j}$ direction. The 0th order variables include the velocity due to the background strain-rate, as well as ϕ_0 and the initial viscosity coefficients, ξ^0, ζ_1^0, ζ_2^0 and ζ_3^0. Due to the normalization, the 0th order shear viscosity and permeability are both 1. The first order shear viscosity coefficient is $\alpha\phi'$, while, to first order, the remaining viscosity coefficients are $\xi^0\alpha\phi'$, $\zeta_1^0\alpha\phi'$, $\zeta_2^0\phi'$ and $\zeta_3^0\alpha\phi'$ where ϕ' is the first order perturbation of the porosity from ϕ_0. The first order permeability perturbation is of the form $k'_\phi = n\phi'/\phi_0$. The porosity perturbation is assumed to take the form $\phi' = \exp(ik_x x + ik_y y + s(t) - i\Omega(t))$ where k_x and k_y are wavenumbers in x and y directions, $s(t)$ characterizes the amplitude and $\Omega(t)$ is the phase of oscillations. Following *Spiegelman* (2003), the wavenumbers are taken to be time-dependent and of the form $k_x = k_{0x}$ and $k_y = k_{0y} - k_{x0}t$. The velocity and pressure perturbations are assumed to be of the form $U' = \tilde{U}\phi'$, $V' = \tilde{V}\phi'$ and $p' = \tilde{p}\phi'$ where a tilde indicates a constant value. With these substitutions, equation 8 can be written

$$\frac{ds}{dt} - i\frac{d\Omega}{dt} = (1-\phi_0)(ik_x\tilde{U} + ik_y\tilde{V}). \tag{10}$$

Equations 6 and 7 can then be written in the following matrix form

$$\begin{pmatrix} k_x & k_y & k^2 \\ -k_y^2(1-\zeta_1^0) - k_x^2\vartheta_1 - 2k_xk_y\zeta_3^0 & -k_xk_y(\xi^0 - 2\zeta_1^0) - k^2\zeta_3^0 & k_x(1+\xi^0) \\ -k_xk_y(\xi^0 - 2\zeta_1^0) - k^2\zeta_3^0 & -k_x^2(1-\zeta_1^0) - k_y^2\vartheta_2 - 2k_xk_y\zeta_3^0 & k_y(1+\xi^0) \end{pmatrix}$$

$$\times \begin{pmatrix} i\tilde{U} \\ i\tilde{V} \\ \tilde{p} \end{pmatrix} = \begin{pmatrix} -ik_ynB_u\frac{1-\phi_0}{\phi_0} \\ \alpha(k_y(1-\zeta_1^0) + k_x\zeta_3^0) \\ \alpha(k_x(1-\zeta_1^0) + k_y\zeta_3^0) - iB_u(1+\xi^0) \end{pmatrix} \tag{11}$$

where $\vartheta_1 = (1+\xi^0+\zeta_1^0+2\zeta_2^0)$ and $\vartheta_2 = (1+\xi^0+\zeta_1^0-2\zeta_1^0)$ and $k^2 = k_x^2 + k_y^2$. Equation 11 can be inverted to find $\tilde{U}$ and $\tilde{V}$ which can be entered into equation 10 to get expressions for the growth rate, $\frac{ds}{dt}$, and instantaneous oscillation frequency, $\frac{d\Omega}{dt}$,

$$\frac{ds}{dt} = \frac{-2\alpha k_xk_yk^2(1-\phi_0)[(1+\zeta_1^0)(k^2(1-\zeta_1^0) + 2k_xk_y\zeta_3^0) + (1-\zeta_1^0)\zeta_2^0(k_x^2 - k_y^2)]}{A+B+C} \tag{12}$$

and

$$\frac{d\Omega}{dt} = \frac{1-\phi_0}{\phi_0} B_u (1+\xi^0)[(n(1-\phi_0)-\phi_0)(1-\zeta_1^0)k_y k^4 + 8\zeta_1^0 k_x^2 k_y^3 n(1-\phi_0) - 2\phi_0 k^2 k_x^2 k_y (2\zeta_1^0 + \zeta_2^0)$$

$$+\zeta_3^0 \phi_0 k_x (k_x^4 - k_y^4)]/(A+B+C). \quad (13)$$

$$A = k^6[(1-\zeta_1^0)(1+\xi^0+\zeta_1^0) - (\zeta_3^0)^2] + 4k_x^2 k_y^2 k^2[(\zeta_3^0)^2 + 2\xi^0\zeta_1^0]$$

$$B = k^4(1-\zeta_1^0)(1+\xi^0) + 8\zeta_1^0(1+\xi^0)k_x^2 k_y^2 + 4k_x k_y k^4(1+\zeta_1^0)\zeta_3^0$$

$$C = 2\zeta_2^0(1-\zeta_1^0)(-k_y^6 + k_x^6 + k_x^4 k_y^2 - k_x^2 k_y^4) - 4(\zeta_2^0)^2 k_x^2 k_y^2 k^2 + 4k_x k_y \zeta_2^0 \zeta_3^0 (k_x^4 - k_y^4) \quad (14)$$

Equation 12 reduces to the form for the growth rate for melt bands with isotropic viscosity which was first derived by *Spiegelman* (2003) when $\zeta_1^0 = \zeta_2^0 = \zeta_3^0 = 0$ if the terms $(1+\xi^0)$ are replaced by $(\xi^0 + 4/3)$. *Takei and Holtzman* (2009a) argued that the former is more appropriate in two dimensions. *Takei and Holtzman* (2009c) also derived a growth rate for melt bands with anisotropic matrix viscosity. They used as a length scale a compaction length of the form $\delta_c = [k_0\eta^0(1+\xi^0-3\zeta_1^0)/\mu]^{0.5}$ rather than $\delta_c = [k_0\eta^0(1+\xi^0)/\mu]^{0.5}$. Their expression gives identical results to equation 12 when either $\zeta_1^0 = 0$, as in type B anisotropy, or when $|k| \gg 1$ since in this limit the growth rate becomes independent of the wavelength or length scale. For rapidly growing bands, $|k| > 1$, so the expressions give very similar results for most cases of interest.

Equation 13 for the oscillation frequency also reduces to the form for isotropic viscosity (*Spiegelman*, 1993; *Butler*, 2009) when the anisotropy coefficients are 0.

5. Results

Near the beginning of the simulations, random heterogeneity with orientation close to the orientation of maximum growth rate increased in magnitude at the expense of the heterogeneity with other orientations. These bands form with wavelength set by the initial heterogeneity. As the simulation progresses, the bands are rotated by the background simple shear flow. While they are in an orientation for growth, the wavelength of the bands increases. When the bands rotate to high angles, where they are no longer growing or are growing more slowly, new bands nucleate on portions of the old bands that are in orientations for rapid growth. This process, and the

increase in wavelength with time or strain is described in *Butler* (2010). The simulations were terminated when the porosity reached 0 or $2\phi_0$ somewhere in the domain.

In figure 3a, the porosity field at a strain of 2.4 for a simulation with isotropic viscosity is shown while in b, a similar plot is shown for a simulation calculated with type A anisotropy at a strain of 5. $B_u = 0$ for all of the simulations shown in this section. At these times, the maximum porosity is roughly twice the initial porosity while the minimum porosity is close to 0. As can be seen, the bands in the simulation with isotropic matrix viscosity are well formed but are at an angle to the shear plane that is slightly greater than 45°. While the growth rate of bands is maximal at 45°, bands are rotated by the background simple shear flow to higher angles. In figure 3b, it can be seen that the bands with type A anisotropic matrix viscosity form at much shallower angles, similar to what is seen in experiments (*Holtzman et al.*, 2003; *Holtzman and Kohlstedt*, 2007).

Power spectra, integrated over all wavelengths, are plotted as a function of angle in figures 4a and b for simulations with isotropic and type A anisotropic viscosity, respectively. Solid black lines give the spectra of the porosity fields shown in figures 3a and b while dotted lines show the growth rate predicted by linear theory. The dash-dot lines show the final amplitude ($\exp(s)$) predicted by linear theory. All curves have been normalized so that their maximum value is 1. The growth rate predicted by linear theory is maximal when $\theta = 45°$ for the isotropic case but the peak amplitude predicted by linear theory is rotated to roughly 70° by the background flow at a total strain of 2.4. The power spectrum from the numerical simulation shows a peak at roughly 60° at time 2.4.

When the viscosity is anisotropic with type A anisotropy, there are two peaks in the growth rate at 15.1° and 74.9° to the shear plane. Bands at low angles to the shear plane are rotated much more slowly than bands at high angles in simple shear flow and the higher angle bands are rapidly rotated past vertical into an orientation where they decay with time while the lower angle bands stay in an orientation for rapid growth for longer. As a result, linear theory predicts that the maximum amplitude at a total strain of 5 will have only a single peak which is rotated to only 20°. As can be seen, the power spectrum calculated from the numerical simulation is very similar to the linear theory prediction.

In figure 4c, I show the power spectrum as a function of angle for a calculation with type B matrix viscosity anisotropy. As can be seen, the power

spectrum calculated from the porosity field for the end of the calculation has a peak at 60° which closely matches the peak growth rate. The peak amplitude predicted by integrating the growth rate for linear theory is at significantly higher angles indicating that nonlinear effects are acting to reduce the angle of the bands so that they are closer to the orientation for maximum growth rate. Repeats with different random initial conditions for each of the above model runs were performed and the angular spectra were similar. For the high angle bands that obtain for the isotropic viscosity calculations and the calculations with type B anisotropy, new sets of bands formed when old ones rotated to high angles where they would start to decay. The growth of these new bands caused rapid shifts in the angular spectra. As a result, it was found to be better to display only single calculations rather than average over many calculations.

As in *Butler* (2009), I define the amplitude of the porosity heterogeneity as

$$Amp = [\frac{\int(\phi_t - \phi_0)^2 dV}{\int(\phi_{t=0} - \phi_0)^2 dV}]^{0.5}. \tag{15}$$

In figure 5, $log(Amp)$ is shown as a function of time for the numerical simulations (solid lines) while the dashed lines show the logarithm of the maximum amplitude as predicted by linear theory and the dotted lines show the maximum growth rate times time. Except for a short time near the beginning of the simulations when the amplitude of the numerical simulations increases very slowly, the linear theory predicts the time evolution of the amplitude reasonably well and the calculation with anisotropic viscosity grows much more slowly than the case with isotropic viscosity.

Eigenvectors of the stress tensor were calculated for all times and all positions throughout the calculations in order to determine the directions of maximum compression and extension when the matrix was strained. The maximum deviation from ±45° was found to increase with increasing strain but the maximum value at the final time was only 4°, indicating that the variations in direction of maximum compression and extension from the background case were small.

5.1. Transition from A to B type anisotropy

In order to model the effect of a changing grain scale melt alignment, some simulations were undertaken for which the viscous anisotropy transitioned continuously from A to B type anisotropy. In figure 6a, I show the viscosity

anisotropy coefficients as a function of time for one of these simulations. The anisotropy coefficients were varied by continuously changing Θ_1 from 0 to 0.2 and Θ_2 from Θ_0^1 to 0.2. In figure 6b I show the power spectrum as a function of time. The power spectrum has been normalized by the maximum power at each time. Although there is a gradual change in the viscous anisotropy coefficients between times of 1 and 2, the power spectrum shows an abrupt change from low angle bands to high angle ones and the final porosity looks very similar to the calculation with type B anisotropy throughout the simulation. Simulations were also undertaken in which the viscous anisotropy transition was very abrupt and the power spectrum as a function of angle and time and the final porosity field were very similar to the case with a gradual transition. Some other simulations were undertaken in which $\Theta_1 = 1/3$ while Θ_2 was decreased continuously from Θ_0^1 to various final values. It was found that as long as Θ_2 was decreased to roughly $2/3\Theta_0^1$ that the bands rotated as shown above, indicating that almost any type B anisotropy near the end of a simulation will result in high angle bands in the final state.

5.2. Effects of Buoyancy

The instantaneous oscillation frequency, $d\Omega/dt$, predicted from equation 13 is plotted in figure 7 for $n = 3$, $\phi_0 = 0.01$ and $B_u = 1$ for calculations with isotropic viscosity (dotted line) as well as type A (solid line) and type B (dashed line) viscosity anisotropy. The oscillation frequency scales linearly with B_u. For the sense of shear flow calculated, positive θ indicates a band dipping to the right while negative θ indicates a band dipping to the left. Porosity waves occur as fluid flow is retarded and enhanced at vertical changes in permeability and the resulting change in fluid pressure opens and closes pore space. As can be seen, for isotropic viscosity, the oscillation frequency peaks for horizontal bands but the peak is shifted to positive angles for the anisotropic viscosity cases and the curves become asymmetric about $\theta = 0$. Unlike the growth rate which is essentially independent of the magnitude of the wavenumber once these are greater than 1, the oscillation frequency depends on the wavenumber magnitude. The magnitudes of the wavenumbers used to calculate the curves in figure 7 were chosen to give the same maximum oscillation frequency and had values 2.15π, 12.76, and $4\sqrt{2}\pi$ for the isotropic case, and the type A and type B anisotropic viscosity cases, respectively.

In figure 8, the quantity $\log(|\phi - \phi_0|)$ at the centre of the solution domain for two simulations is shown. The curves have been offset by 5 in order to separate them. The upper solid curve is from a calculation using type B anisotropy with initial condition $\phi = \phi_0 + \Delta\phi \cos(4\pi x + 4\pi y)$ (i.e. bands oriented at 45° to the shear plane with wavenumber $4\sqrt{2}\pi$). The lower solid curve is from a simulation with type A anisotropy with plane waves oriented at 10° to the shear plane with wavenumber magnitude 12.76 as the initial condition. The dotted lines indicate curves of $s + \log(|\cos(\Omega)|)$ for s and Ω calculated from numerical integration of equations 12 and 13 with the same viscosity parameters and initial conditions as the numerical simulations. As can be seen, for the calculation with type A anisotropy, the increase of the amplitude of the porosity deviation from ϕ_0 is well approximated by linear theory throughout the simulation while the oscillations for the linear theory and numerical simulations are in phase for roughly the first 0.8 of the simulation. For the type B anisotropy calculation, the initial plane wave perturbation was at a steeper angle which was rotated by the background flow to vertical at time 1. When bands are rotated beyond vertical, the porosity heterogeneity will decrease with time as can be seen by the linear theory prediction. The bands in the numerical simulation continue to grow in amplitude because the bands break and new bands nucleate on heterogeneity that is at an orientation for rapid growth in a manner similar to the "pumping" mechanism described by *Holtzman and Kohlstedt* (2007) and seen also in the models of *Katz et al.* (2006). As can be seen, roughly the first four oscillations are well predicted by the numerical model for the type B viscosity anisotropy case. The oscillation frequency depends on both the orientation of the bands as well as their wavelength. For the type A viscosity anisotropy, it can be seen from figure 7 that the initial oscillation frequency was 35 and would increase as the band was rotated to steeper angles, until it reaches a maximum at 24°. In the calculation shown in figure 8, the bands only rotate to 15^o. The magnitude of the wavenumber is also decreasing which also increases the oscillation frequency. These effects can be seen in the decreasing period of oscillation for the type A case seen in figure 8. For the type B case, the initial oscillation frequency at the initial orientation of 45° is 28 and will decrease as the bands are rotated to higher angles. This is particularly evident in the linear calculation where bands get rotated to 135°. Although the period of oscillation clearly increases in the nonlinear simulation, the increase is not as large since the bands break and reform at angles more favorable for growth.

In figure 9a the porosity and fluid velocity (magenta arrows) fields are shown at time 4.23 for a calculation run with $B_u = 10$, a random initial condition, and type A viscous anisotropy. Rapid oscillations of the porosity bands were seen in the time evolution of this calculation. The growth rate of the porosity localization was similar to calculations without buoyancy as was found by *Butler* (2009) for isotropic viscosity calculations. As can be seen, the low angle bands are still present but they have a shorter wavelength than those with no buoyancy (compare to figure 3b) and a second set of bands at higher angles is also seen. The dashed line in figure 4b gives the amplitude spectrum as a function of angle for the porosity field seen in figure 9a and the power at the high-angle band can be clearly seen and is in rough agreement with the high angle for rapid growth predicted by linear theory. This is similar to what is seen for strain-rate dependent isotropic viscosity calculations with buoyancy (*Butler*, 2009). *Butler* (2010) showed that buoyancy induced oscillations reduce the increase of band wavelength with time for calculations with isotropic viscosity. Bands increase in wavelength because their wavelength increases during rotation by the background flow when they are in an orientation for growth (*Butler*, 2010). Similarly, the high angle bands for the type A viscosity anisotropy and for the strongly strain-rate dependent isotropic calculations are not seen when buoyancy is not present because these are rapidly rotated to an orientation where the will decay with time (*Katz et al.*, 2006). When there is strong buoyancy, many little pockets of high and low porosity form because of the waves. As a result, there are many new nucleation sites for bands and new bands are constantly forming in directions favorable for growth. As a result, when buoyancy is strong, high angle bands are present and the increase in band wavelength due to rotation by the background flow does not occur. Calculations with $B_u \leq 1$ showed behaviour that was very similar to the $B_u = 0$ cases.

In figure 9b, the porosity field at time 1.8 is shown for a calculation with type B anisotropy and $B_u = 10$. For this type of anisotropy, there is a single peak in the growth rate at around 60° (see figure 4c) and the observed bands are close to this angle. The spacing of the bands in this calculation also is reduced compared with another calculation with no buoyancy (not shown) and the growth rate of these bands is very close to the prediction of linear theory and to the growth rate for bands with no buoyancy. Because the bands are close to vertical in this case, the fluid velocity can be seen to be channelized into the high porosity bands.

6. Discussions and Conclusions

The numerical modeling results indicate that melt bands form at low angles to the shear plane if the matrix viscosity is anisotropic as would occur if the grain-scale melt were aligned in long pockets parallel to the direction of maximum compression. If the grain-scale melt pockets reorient to low angles themselves, as is observed in laboratory experiments at high strain, then the simulated bands are seen to rapidly reorient to high angles. As a result, anisotropic viscosity can explain why bands start to form at low angles but another mechanism is required to keep them at low angles in highly strained experiments. *Takei and Holtzman* (2009c) came to essentially the same conclusion based on their linear theory.

When the melt is buoyant, the wavelength of the bands is reduced and when the matrix viscosity has type A anisotropy, a second orientation of bands is seen that is at an angle that is similar to the second direction of maximum growth rate. As was shown for strain-rate dependent isotropic viscosity by *Butler* (2009), this second set of bands would reduce the efficiency of melt channelization towards the ridge axis.

In the current study, the viscous anisotropy is set based on experimental observations of the orientation of melt at the grain scale. Although *Takei and Holtzman* (2009b) were able to predict the occurrence of type A anisotropy self consistently, a complete self consistent model that can predict viscous anisotropy as a function of the stress field has still not been obtained (*Takei and Holtzman*, 2009c). It will also be noted that in our model, the magnitude of the viscous anisotropy is assumed to be constant, which is consistent with the viscous anisotropy being "stress-saturated". Future studies may also consider the effects of rotation of the axis of viscous anisotropy as the viscosity becomes more heterogeneous.

In the simulation results shown here, and those of *Katz et al* (2006) as well as *Butler* (2009,2010), the bands for any given simulation at any given time have similar wavelengths and do not form networks. In contrast, in experimental investigations (e.g. *Holtzman et al.*, 2003) bands of many different wavelengths form an interconnecting network. In the experiments of *Holtzman et al.* (2003) strain markers were seen to be significantly offset at the positions of the bands and *Holtzman et al.* (2003, 2005) have proposed that strain is concentrated in the porosity-rich bands and that the connections between different bands allows for strain partitioning. That the eigenvectors of the stress tensor only deviated by 4° from the principle strain-rate axes of the

background flow is an indication that the stress field was not strongly affected by the viscosity heterogeneity in our calculations and that strain-partitioning was not taking place. Another way of determining whether strain partitioning is taking place is to look at the perturbation vorticity field ($\frac{\partial V}{\partial x} - \frac{\partial U}{\partial y}$). If strain is concentrated in high porosity bands then the perturbation vorticity field should correlate with the high porosity bands. *Katz et al.* (2006) plotted these fields for a calculation with strongly-strain rate dependent viscosity and found that they did not strongly correlate. Similar calculations with type A anisotropy were carried out during this investigation (not shown). Although the perturbation vorticity field tended to be high within the melt-rich bands, it was also high in the melt-poor lenses. A few simulations were undertaken with initial porosity of 0.1. When the initial porosity is increased, the final difference in viscosity between the melt-rich bands and the melt-poor lenses is increased. In these calculations, the perturbation vorticity was significantly correlated with the melt rich bands indicating that strain-partitioning was occurring. An interconnecting network of bands did not form, however. *Holtzman and Kohlsted* (2007) showed experiments where the porosity was as high as three times its initial value in the bands while in the calculations shown here the final maximum porosity was roughly two times the initial value. It is possible that a higher amplitude of melt segregation is necessary in order for strain partitioning to occur. Alternatively, it is possible that the physics in the experimental systems that allows them to create connected networks that strongly partition strain is not present in the continuum simulations. Strong strain partitioning may also be what is needed to stabilize the bands at low angles once the grain-scale melt pockets realign at low angles.

In a future study, I will investigate how anisotropic matrix permeability affects band formation. *Hier-Majumder* (2011) estimated that permeability would be greater by a factor of ten in a direction parallel to melt pockets as compared with perpendicular to them at stresses appropriate to the upper mantle. When melt pockets are parallel to the direction of maximum compression, this should impede melt band development since fluid flow that is necessary to produce bands would need to occur in the direction of reduced permeability. I expect that this will reduce the growth rate of bands and may lead to lower angle bands. This effect might be expected to be greater for the greater stresses associated with laboratory experiments.

7. References

1. Butler, S.L., The effects of buoyancy on shear-induced melt bands in a compacting porous medium, *Phys. Earth Plan. Int.*DOI 10.1016/ j.pepi.2008.10.022, *173*, 51-59, 2009.
2. Butler, S.L., Porosity Localizing Instability in a Compacting Porous Layer in a Pure Shear Flow and the Evolution of Porosity Band Wavelength, *Phys. Earth Plan. Int.*, *182*, doi:10.1016/j.pepi.2010.06.004, 30-41, 2010.
3. Daines M., and D. Kohlstedt, Influence of deformation on melt topology in peridotites, *J. Geophys. Res.*, *102*, 10 257-10 271, 1997.
4. Forsyth, D., D. S. Scheirer, S. C. Webb et al. Imaging the deep seismic structure beneath a mid-ocean ridge: the melt experiment, *Science*, *280*, 1215-1218, 1998.
5. Hier-Majumder S., Development of anisotropic mobility during two-phase flow, *Geophys. J. Int.*, *186*, 59-68, DOI: 10.1111/j.1365-246X.2011.05024.x, 2011.
6. Holtzman B.K., Kohlstedt D.L., Stress-driven melt segregation and strain partitioning in partially molten rocks: Effects of stress and strain, *Jour. of Petrol.*, *48*, 2379-2406, 2007.
7. Holtzman, B.K., D.L. Kohlstedt and J. Phipps Morgan, Viscous Energy Dissipation and Strain Partitioning in Partially Molten Rocks, *Jour. of Petrol.*, *46*, 2569-2592, 2005, doi:10.1093/petrology/egi065.
8. Holtzman, B., Groebner, N., Zimmerman, M., Ginsberg, S., Kohlstedt, D., Stress-driven melt segregation in partially molten rocks, *Geochem. Geophys. Geosyst.*, *4*, Art. No. 8607, 2003.
9. Katz R.F., Porosity-driven convection and asymmetry beneath mid-ocean ridges. Geochem. Geophys. Geosys., 10(Q0AC07), 2010. doi: 10.1029/2010GC003282.
10. Katz R.F., Spiegelman M., Holtzman B., The dynamics of melt and shear localization in partially molten aggregates, *Nature*, *442*, 676-679, 2006.
11. Kelemen P.B., Hirth G., Shimizu N.,Spiegelman M., Dick H.J.B., A review of melt migration processes in the adiabatically upwelling mantle beneath oceanic spreading ridges, *Phil. Trans. Roy. Soc. A*, *355*, 283-318, 1997.

12. King D.S.H., Zimmerman M.E. and D. L. Kohlstedt, Stress-driven Melt Segregation in Partially Molten Olivine-rich Rocks Deformed in Torsion, *Jour. of Petrol.*,*51*, 21-42, doi:10.1093/petrology/egp062, 2010.
13. Kohlstedt D.L. and B. K. Holtzman, Shearing Melt Out of the Earth: An Experimentalist's Perspective on the Influence of Deformation on Melt Extraction, *Ann. Rev. Earth and Planet. Sci. 37*, 561-593, doi:10.1146/annurev.earth.031208.100104, 2009.
14. Kohlstedt, D.L., Zimmerman M.E. and S. J. Mackwell, Stress-driven Melt Segregation in Partially Molten Feldspathic Rocks, *Journ. of Petrol.*, doi:10.1093/petrology/egp043, 2009.
15. McKenzie, D., The Generation and Compaction of Partially Molten Rocks, *Jour. Petrol.*, *25*, 713-765, 1984.
16. Mei, S., Bai, W., Hiraga, T., Kohlstedt, D., Influence of melt on the creep behavior of olivine-basalt aggregates under hydrous conditions, *Earth Planet Sci. Lett.*, *201*, 491-507, 2002.
17. Rabinowicz M., Vigneresse J.L., Melt segregation under compaction and shear channeling: Application to granitic magma segregation in a continental crust, *Jour. Geophys. Res.*, *109*, doi:10.1029/2002JB002372, 2004.
18. Ricard, Y., Bercovici, D. and Schubert, G. A two-phase model for compaction and damage 2. Applications to compaction, deformation, and the role of interfacial surface tension, *J. Geophys. Res.*, *106*, 8907-8924, 2001.
19. Richardson, C. Melt flow in a variable viscosity matrix, *Geophys. Res. Lett.*, 25, 1099-1102, 1998.
20. Scott, D.R, and Stevenson, D.J., Magma Solitons, *Geophys. Res. Lett.*, *11*, 1161-1164, 1984.
21. Spiegelman, M., Linear analysis of melt band formation by simple shear, *Geochem. Geophys. Geosys.*, *4*, Article 8615, doi:10.1029/2002GC000499, 2003.
22. Spiegelman, M., Flow in deformable porous media. Part 1 Simple analysis, *Jour. Fluid Mech.*, *247*, 17-38, 1993.
23. Stevenson, D., Spontaneous small-scale melt segregation in partial melts undergoing deformation, *Geophys. Res. Lett.*, *16*, 1067-1070, 1989.
24. Takei, Y., Deformation-induced grain boundary wetting and its effects on the acoustic and rheological properties of partially molten rock analogue, *J. Geophys. Res.*, *110*, B12203, doi:10:1029/2005JB, 2005.

25. Takei Y., Stress-induced anisotropy of partially molten rock analogue deformed under quasi-static loading test, *J. Geophys. Res.*, *115*, B03204 DOI: 10.1029/2009JB006568, 2010.
26. Takei Y, Holtzman B., Viscous constitutive relations of solidliquid composites in terms of grain boundary contiguity I: Grain boundary diffusion-control model, *J. Geophys. Res.*, *114*, B06205. doi:10.1029/2008JB005850, 2009
27. Takei Y, Holtzman B., Viscous constitutive relations of solid-liquid composites in terms of grain boundary contiguity: 2. Compositional model for small melt fractions, *114*, B06206, DOI: 10.1029/2008JB005851, 2009.
28. Takei Y, Holtzman B., Viscous constitutive relations of solid-liquid composites in terms of grain boundary contiguity 3: Causes and consequences of viscous anisotropy, *J. Geophys. Res.*, *114*, B06207, doi:10.1029 /2008JB005852, 2009.
29. Vera, E.E., Mutter J.C., Buhl, P., et al., The Structure of 0-MY to 0.2-MY old oceanic-crust at 9-degrees-n on the east pacific rise from expanded spread profiles, *Jour. Geophys. Res.*, *95*, 15529-15556, 1990.
30. Wark D.A., Watson E.B. Grain-scale permeabilities of texturally equilibrated, monomineralic rocks, *Earth Plan. Sci. Lett.164*, 591605, 1998.
31. Zimmerman, M., S. Zhang, and D. Kohlstedt, Melt distribution in mantle rocks deformed in shear, *Geophys. Res. Lett.*, *26*, 1505-1508, 1999.

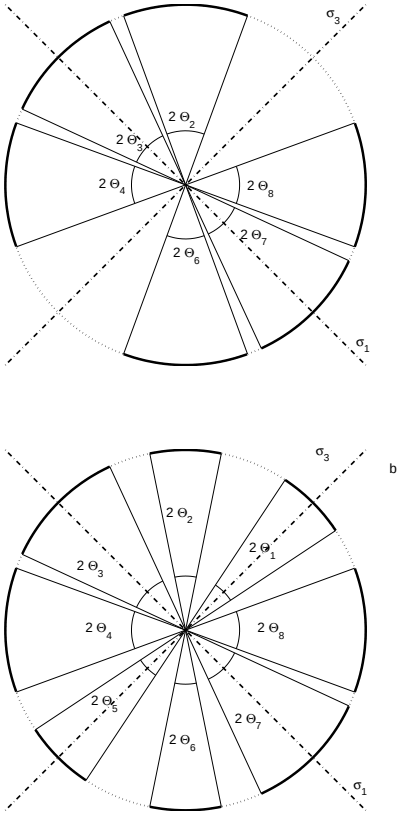

Figure 1: a) The regions of contact around a circular grain as characterized by the angles Θ_k. For this case representing type A anisotropy, $\Theta_1 = 0$ describing long melt pockets parallel to the σ_1 direction. b) The regions of contact around a circular grain for type B anisotropy with reduced Θ_1 and Θ_2 describing long melt pockets at 20° to the shear plane. σ_1 is the orientation of maximum compressive stress for the simple shear flow used here while σ_3 is the orientation of maximum extension.

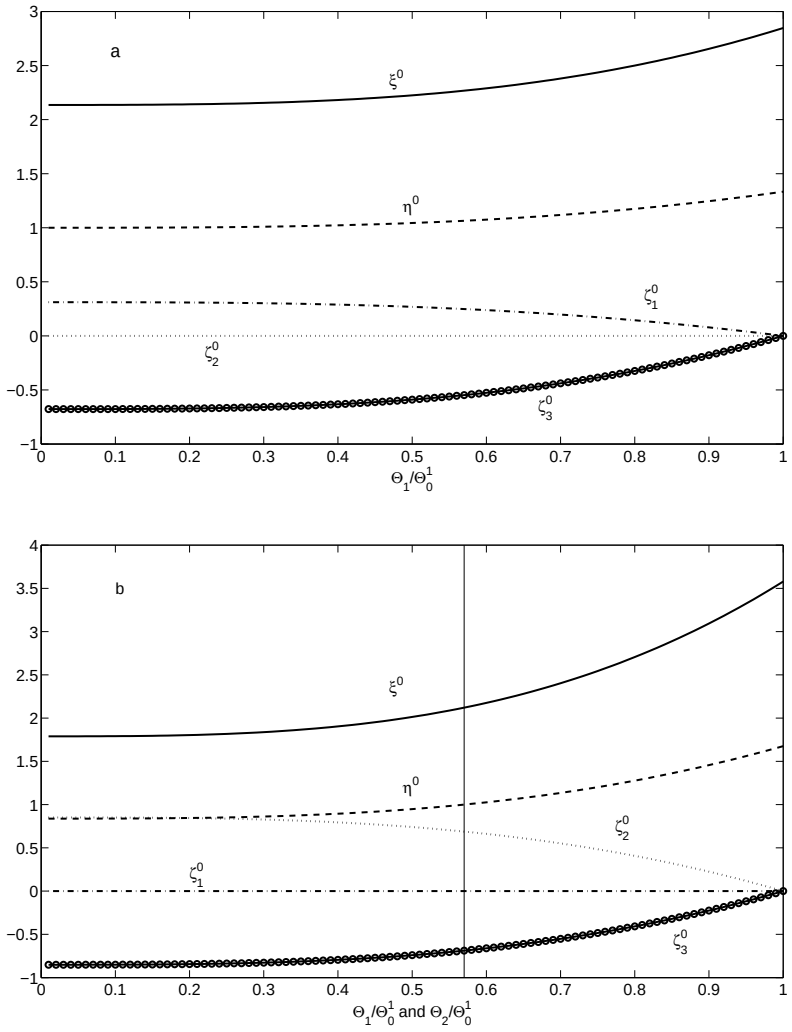

Figure 2: a) The variation of the viscosity coefficients with Θ_1/Θ_0^1 (type A anisotropy). Curves have been normalized by the value of η^0 at $\Theta_1 = 0$. b) The variation of the viscosity coefficients with $\Theta_1/\Theta_0^1 = \Theta_2/\Theta_0^1$ (type B anisotropy). Curves have been normalized by the value of η^0 at $\Theta_1 = \Theta_2 = 0.2$ when $\Theta_0^1 = 0.3512$.

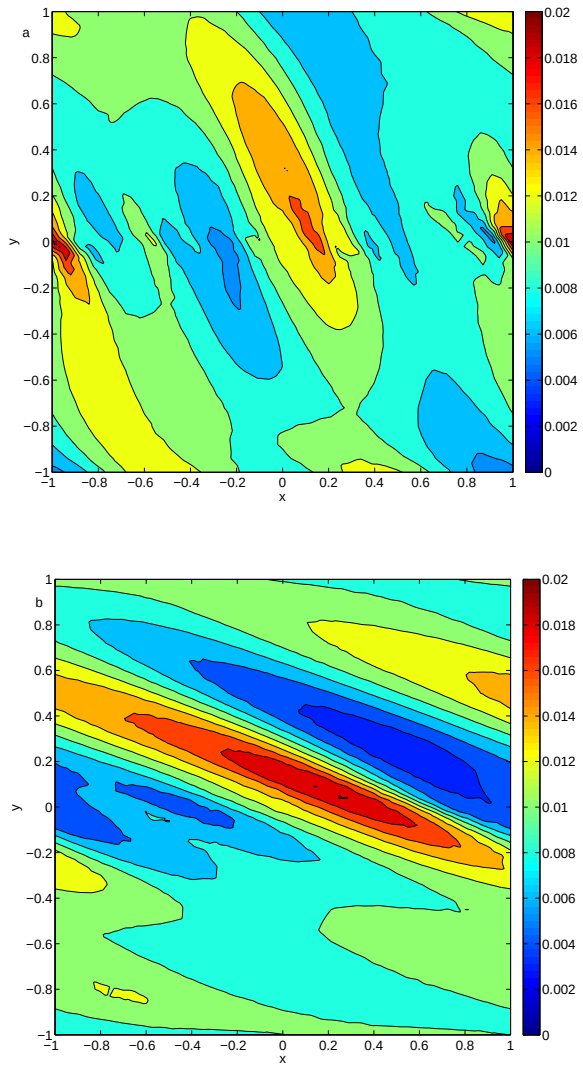

Figure 3: Color plots of the final porosity field for calculations with $B_u = 0$ and a random initial condition. Part a) shows the results for isotropic matrix viscosity at time 2.4 while part b) shows the results of a simulation with type A anisotropic viscosity at time 5.

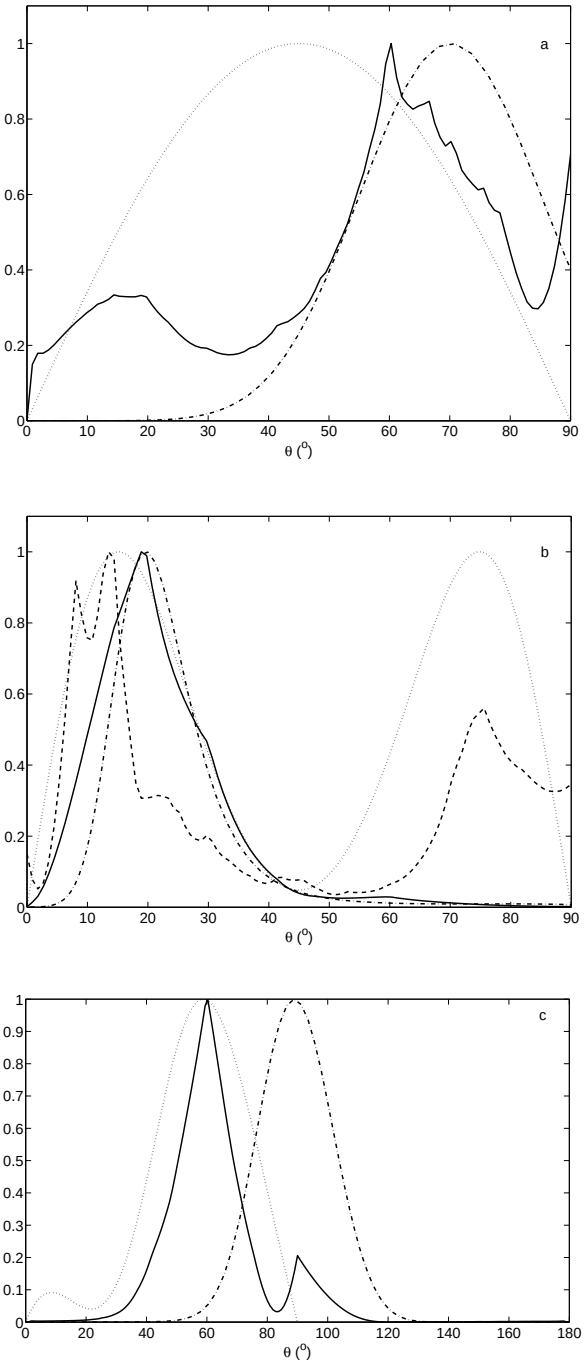

Figure 4: Dotted and dash-dotted lines show the growth rate and final amplitude as a function of angle as predicted by linear theory. Figure a shows the power spectrum as a function of angle for the calculation with isotropic viscosity at the final time (solid line) b shows the power spectrum as a function of angle for the simulation with anisotropic viscosity of type A at the final time with $B_u = 0$ (solid line) and $B_u = 10$ (dashed line). c the power spectrum for a calculation with type B anisotropy.

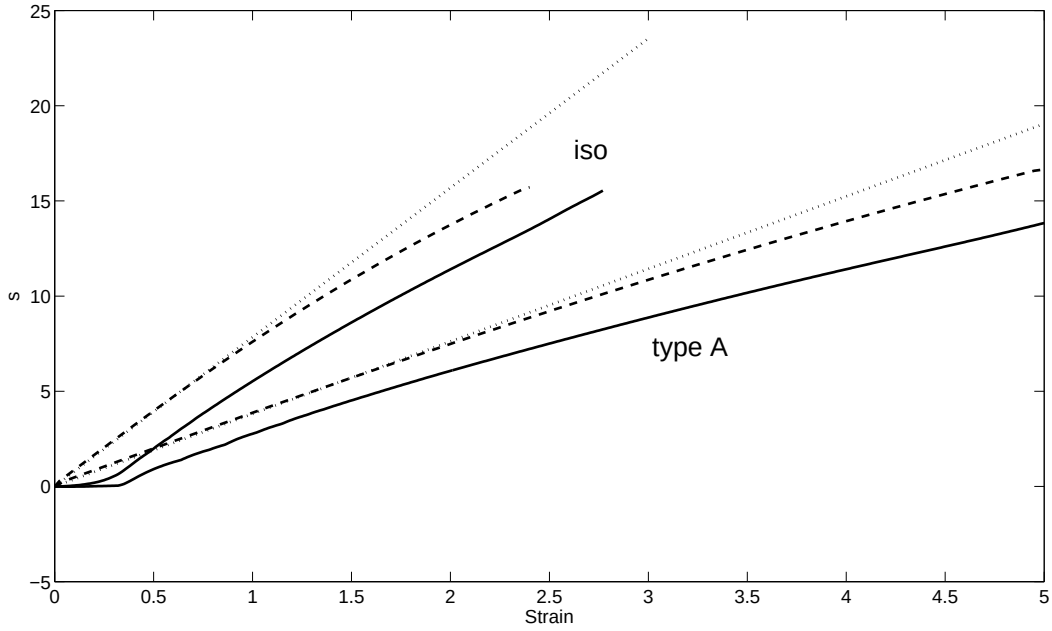

Figure 5: The maximum growth rate as predicted by linear theory times time (dotted line), the maximum logarithmic amplitude as predicted by linear theory (dashed line) and the logarithmic amplitude computed from the numerical simulations (solid line). The upper set of curves are for the simulation with isotropic viscosity while the lower set are for simulations with type A anisotropic viscosity.

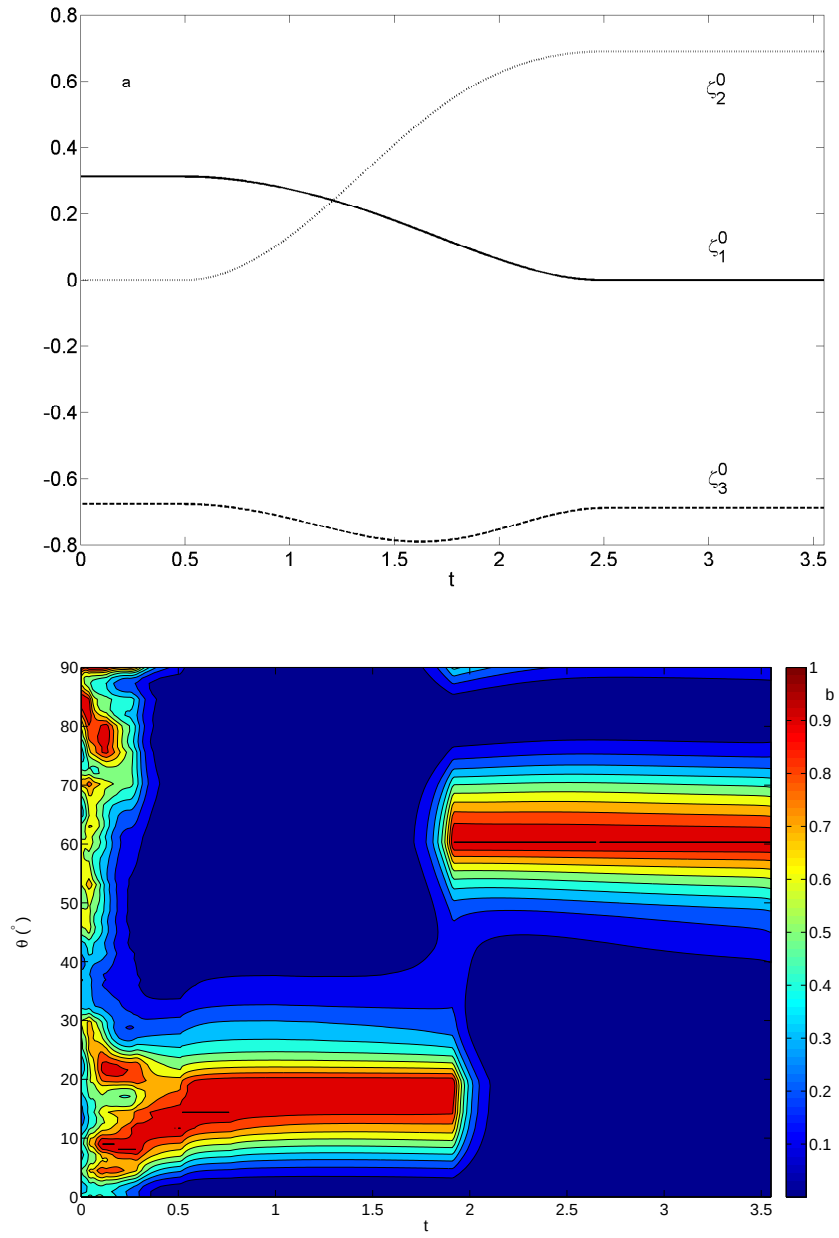

Figure 6: a) Viscosity coefficients as a function of time for a calculation where the matrix viscosity changes from type A to type B anisotropy. b) The power spectrum as a function of angle and time for a calculation employing the viscosity anisotropy coefficients shown in part a.

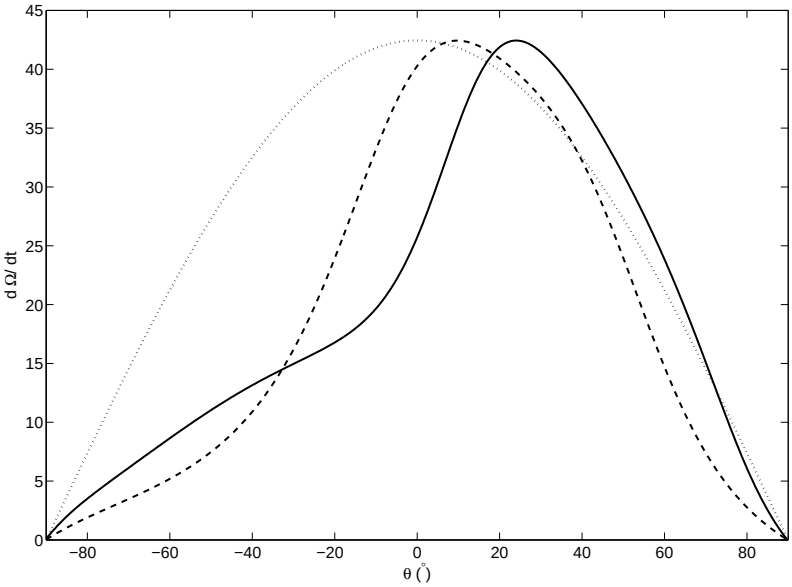

Figure 7: The oscillation frequency as a function of band orientation for the isotropic (dotted line), type B anisotropy (dashed line) and type A anisotropy (solid line) cases. The initial magnitude of the wavenumber was 2.15π, 12.76 and $\sqrt{2}4\pi$ for the isotropic viscosity, type A and type B viscous anisotropy calculations. For all of these calculations, $B_u = 1$, $\phi_0 = 0.01$ and $n = 3$.

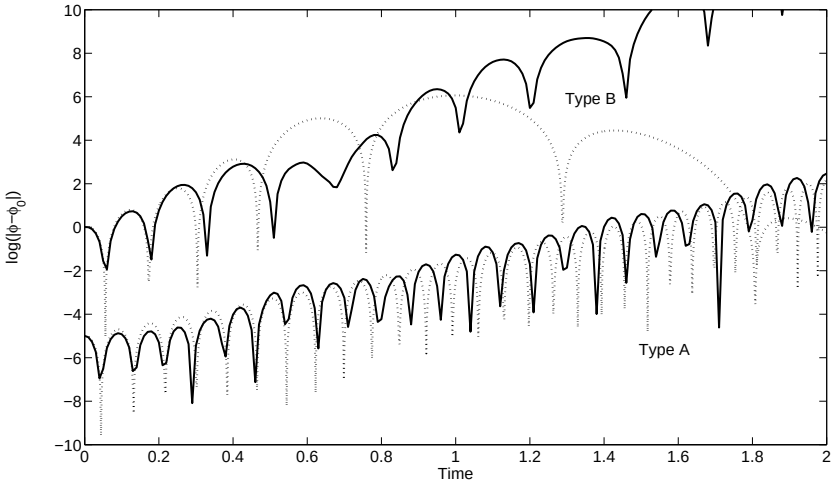

Figure 8: Logarithmic change in the porosity field at the centre of the calculation domain for a calculation with type B viscous anisotropy, $B_u = 1$, and with initial condition $\phi - \phi_0 = \Delta\phi \cos(4\pi x + 4\pi y)$ (upper solid curve) and with type A anisotropy, $B_u = 1$, starting with a plane wave perturbation at 10^0 to the shear plane (lower solid curve). The dotted curves show the results calculated from the expression $s + \log(|\cos(\Omega)|)$ with s and Ω calculated from numerical integration of equations 12 and 13 for the same parameters as the numerical solutions.

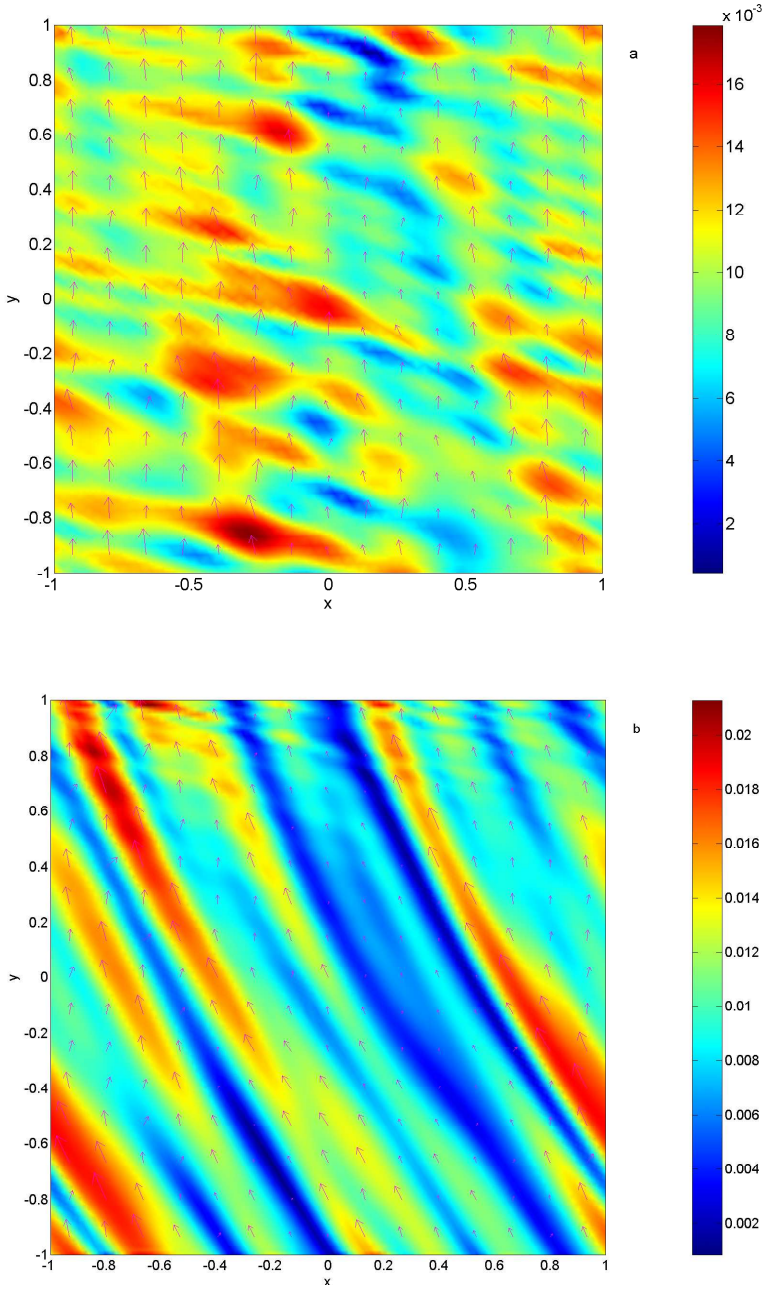

Figure 9: a) Porosity field at time 4.23 for a calculation with type A matrix viscosity anisotropy with $B_u = 10$ and a random initial condition. b) Porosity field at time 1.8 for a calculation with type B anisotropy with $B_u = 10$ and a random initial condition. The magnenta arrows indicate the fluid velocity.